Numerical simulation and analysis of hybrid physical-chemical vapor deposition to grow uniform perovskite MAPbI₃

Chongqiu Yang ⓘD, Terrence Simon, and Tianhong Cui

View Online   Export Citation   CrossMark

ARTICLES YOU MAY BE INTERESTED IN

121, 144903

AIP
Publishing

Numerical simulation and analysis of hybrid physical-chemical vapor deposition to grow uniform perovskite MAPbI₃

Chongqiu Yang,[1,2] Terrence Simon,[2] and Tianhong Cui[2,a)]

[1]*School of Mechatronics Engineering, Harbin Institute of Technology, Harbin 150001, China*
[2]*Department of Mechanical Engineering, University of Minnesota, Minneapolis, Minnesota 55455, USA*

Applications of metal halide perovskite have been rapidly developing in recent years. However, very little research focusing on basic growth kinetics of perovskite films can be found in the literature. This paper discusses a hybrid physical-chemical deposition process of planar perovskite films. A 2-D ANSYS Fluent simulation is presented to calculate the heat and mass transfer during the deposition process. An optimized mass flow configuration with a flow resistance imposed by a porous screen is shown to give a uniform distribution of the methylammonium iodide vapor precursor and an even surface deposition rate of perovskite films. Both steady and transient calculations indicate that increasing operating temperature or vessel pressure within certain limits can boost the surface deposition rate of perovskite. Limitations on working pressure are presented for preventing reverse flow into the chamber and associated deterioration of deposition uniformity of the perovskite films. *Published by AIP Publishing.*
[http://dx.doi.org/10.1063/1.4980116]

I. INTRODUCTION

Metal halide perovskite photovoltaic absorbers for solar cells have drawn tremendous attention due to their excellent properties, such as tunable bandgap, very long carrier diffusion length, easy-processing, and low-cost. The Power Conversion Efficiency (PCE) of perovskite solar cells has rapidly improved from 3.8% to 22.1% in recent years.[1–3] From dye sensitized solar cells[2] to the present mesoporous structure,[4] planar heterojunction structure,[5] and inverted planar structure,[6] perovskite solar cells have demonstrated great potential to compete with commercialized silicon solar cells, especially the planar perovskite solar cells. Although the mesoporous perovskite solar cells hold the record for PCE, the planar perovskite solar cells are expected to become the dominant architecture if the deposition process and interface engineering can be enhanced.[7]

With the development in the past few years, morphology control of the deposited perovskite thin films has had a crucial influence on photovoltaic performance. To realize uniformly dense perovskite films with fewer defects, a variety of methodologies have been developed,[8] such as one-step spin coating, sequential deposition with spin coating, immersion or vapor-assisted coating, and vacuum dual-source vapor deposition. Although extremely high efficiencies were achieved by the solution process, the uncertainties in the solution process make the refabrication of large-area perovskite modules for commercial purposes challenging. In contrast, the vapor-assisted deposition technique is beneficial for effectively controlling the working temperature, pressure, heat, and mass transfer and preventing excessively fast reactions among perovskite precursor materials. In addition, due to the boiling point differences of precursor organic and inorganic materials, the vapor-assisted coating method is simpler and more controllable than the dual-source vapor deposition process. Therefore, the vapor-assisted hybrid physical-chemical deposition method is considered to be a promising approach to achieving large and uniform perovskite thin films.

The vapor-assisted two-step deposition process was first reported in 2013 by Yang's group.[9] They annealed the PbI₂ substrate in CH₃NH₃I (MAI) vapor at 150 °C within an N₂ atmosphere for 2 h to form full coverage of a perovskite film on a compact TiO₂ layer, achieving minimal roughness and large grain sizes, up to a micron scale, giving a PCE of up to 12.1%. Based on this pioneering work, many enhanced approaches were further developed to improve the gas-solid crystallization process and solar cell performance.[10] The PCE of 16.8% for vapor-assisted, mixed perovskite CH₃NH₃PbI₃₋ₓClₓ solar cells was achieved by annealing the mixed lead halide (PbI₂ + PbCl₂) substrate in an MAI vapor atmosphere at 120 °C for 2 h under a low pressure of ∼0.3 Torr. The performance was highly repeatable.[10] Lower pressures could decrease the boiling point of the solid MAI powder, reducing the sublimation temperature. In previous work,[11,12] with a high vacuum of 2 mTorr, the MAI vapor would sublimate at 73 °C and react with a PbI₂ precursor film coated on a mesoporous TiO₂ layer. The highest PCE of 14.7% was later realized when operating at 82 °C. Recently, an efficient all-vacuum-deposited perovskite solar cell with a PCE of up to 17.6% was achieved by precisely controlling the reagent partial pressure in the range of 10^{-5}–10^{-3} Torr.[13] Another modified vapor-assisted deposition method using a commercial heat gun with the controlled temperature and flow rate was developed, exhibiting an excellent PCE of over 18% and superior tolerance to ambient humidity.[14] These research findings show that formation of uniform and stable perovskite films is strongly dependent on control of processing temperature and pressure. Modeling in the present paper addresses the need for a systematic investigation of the parameter space in search of improved performance.

a)Author to whom correspondence should be addressed. Electronic mail: tcui@me.umn.edu

The main obstacle to fabricate planar perovskite films when using the sequential vapor-assisted deposition method is the incomplete conversion of precursor material into perovskite and nonuniform growth of crystalline grains. Presently, most research studies are mainly focused on experimental tests.[15–17] However, to deeply understand and promote the vapor-assisted deposition process, the basic reaction kinetics and heat and mass transfer processes, as affected by operating conditions, must be documented. This information is used for controlling the working conditions when depositing perovskite films. Computational Fluid Dynamics (CFD) can empower the investigation to go further and faster toward improved deposition techniques. ANSYS Fluent contains broad capabilities in physical modeling of mass flow, heat transfer, and reactions. Numerical simulation of the vapor deposition of perovskite films using Fluent is an effective method to deeply understand their growth dynamics. The simulation analysis can be used to achieve optimum working conditions prior to verification experiments, to produce uniform perovskite films with excellent reproducibility and stability. Experience has shown that uniform growth is critical to producing defect-free perovskite films. Thus, simulation is critical to realizing outstanding performance of perovskite solar cells.

In this work, hybrid physical-chemical vapor deposition of planar methylammonium lead iodide (MAPbI$_3$) perovskite films is investigated with a lead iodide (PbI$_2$) substrate and methylammonium iodide (MAI) precursor vapor. It is simulated by utilizing ANSYS Fluent software with a chemical vapor deposition calculation module. An efficient deposition fixture configuration is presented. The geometry is a relatively compact box with three vapor inlet sources and one outlet. The results show a uniform surface deposition rate of perovskite films when a uniform mass flux is imposed from the inlets. It demonstrates how a properly chosen porous screen embedded into the vapor flow path can force the vapor flow to have a more uniform distribution, resulting in a more even surface deposition rate of perovskite films. The influences of operating conditions on the deposition process are quantified using the ANSYS Fluent steady and transient calculations. The results show that the deposition rates of perovskite films increase gradually with increasing working temperature and pressure. The sublimation rate of vapor MAI is simultaneously boosted by raising the temperature and balancing its consumption on perovskite films. However, with increasing working pressure, the sublimation rate of vapor MAI reduces gradually, deteriorating the vapor MAI supply to the increasing deposition rate of perovskite films. When the working pressure exceeds a critical point, the deposition rate of perovskite films surpasses the sublimation rate of vapor MAI, and a backflow develops at the outlet, a condition that should be avoided.

II. SIMULATION MODEL AND BOUNDARY CONDITIONS

Figure 1(a) presents the physical model, a quartz box inside a chamber that is heated by surrounded heating elements to realize an isothermal environment. The chamber is first evacuated to a desired pressure. Next, nitrogen (N$_2$) is
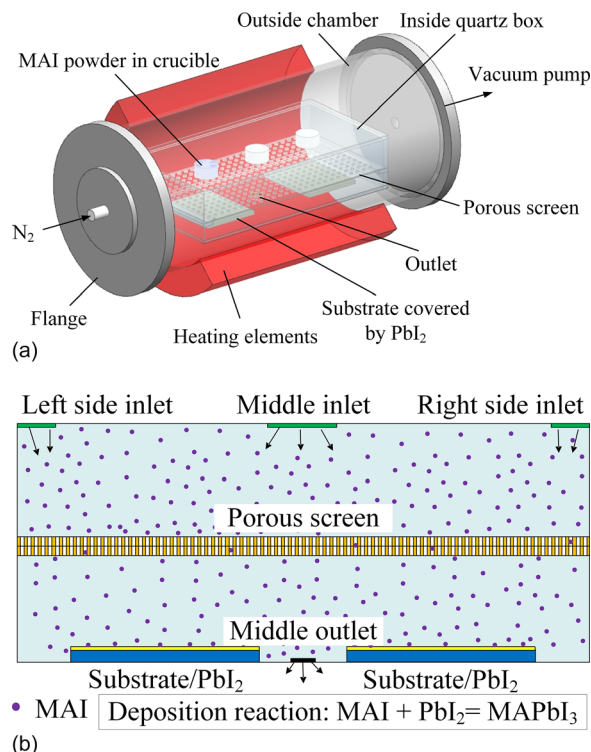

FIG. 1. (a) 3-D physical model and (b) 2-D simulation model in ANSYS Fluent.

introduced into the chamber for 20 min to purge particles and atmospheric gases. The inside quartz box is also purged and evacuated through the outlet at its bottom. After shutting down the N$_2$ flow, the heating element is turned on, and the quartz box is heated to a specific temperature, while the low vacuum pressure is maintained. During the heating process, the MAI powder in the crucible sublimates into the quartz box, mixes and diffuses with N$_2$. The mixture of MAI and N$_2$ flows through the porous screen (Figure 1(a)) to the substrate surfaces below and to the outlet. As the MAI powder continues to sublimate, the quartz box becomes filled with MAI vapor excluding N$_2$, finally reaching a steady state with the stable outlet flow and deposition rate of perovskite films on the substrate surfaces.

To simulate the fluid flow, mass and heat transfer, and reaction rate features of this deposition process, the 2-D ANSYS Fluent model shown in Figure 1(b) was developed. A pressure-based solver is used to iterate on the momentum equation calculation with gravitational acceleration included. A laminar viscous model is chosen, as the Reynolds number is small due to the slow vapor flow rate. Species transport and reactions are included in the chemical vapor deposition model. The quartz box is initially filled with 100% N$_2$. The boundary condition of outlet is set to be pressure-outlet, with constant operating pressure and temperature. The vapor MAI can flow through the outlet, based on its computed concentration and pressure. Cases with reverse flow can be computed, but operation under such conditions is to be avoided.

A stable and uniform mass flux of sublimated MAI vapor is applied as the boundary condition at the three inlets. The sublimation flux is critically related to working

temperature and pressure according to the Knudsen-Langmuir equation[18,19]

$$\frac{dm}{dt} = \alpha(P_{sat} - P)\sqrt{\frac{M}{2\pi RT}}(\text{g cm}^{-2}\,\text{s}^{-1}), \quad (1)$$

where α is a condensation coefficient, P_{sat} is the saturation vapor pressure in bars, P is the working pressure, M is the molecular weight, R is the gas constant which is 83.2×10^6 (erg·K^{-1}·mol^{-1}). In many cases, every incident atom or molecule condenses so that the value of α is unity.[19] The saturation vapor pressure of powder MAI at a specific temperature can be calculated by using the Clausius-Clapeyron equation[20]

$$\ln\frac{P_{sat2}}{P_{sat1}} = -\frac{\Delta H}{R}\left(\frac{1}{T_2} - \frac{1}{T_1}\right), \quad (2)$$

where ΔH is the enthalpy of sublimation of MAI. Dualeh et al.[20] used thermogravimetric analysis to test the sublimation of MAI. They noted that the sublimation temperature of MAI is $247 \pm 26\,°C$ at 1 atmosphere pressure, and the corresponding enthalpy of sublimation is $105 \pm 5\,\text{kJ}\cdot\text{mol}^{-1}$. The saturation vapor pressure at any temperature can be attained using Equation (2), and the sublimation rate can then be calculated by Equation (1) with respect to any working temperature and pressure, as listed in Tables I and II.

Fick's law, including the Soret effect,[21] is adopted to define the mass diffusion flux in a laminar flow of vapor MAI or N_2 inside the box, including that which permeates into the PbI_2 substrate surface. It is described by Equation (3), where J_i is the diffusion flux of a species, ρ is the mixture density, $D_{i,m}$ is the isothermal mass diffusion coefficient[22] for species i in the mixture, $D_{T,i}$ is the thermal diffusion coefficient (Soret effect)[21] for species i, Y_i is the mass fraction of species i, and T is the temperature

$$J_i = -\rho D_{i,m}\nabla Y_i - D_{T,i}\frac{\nabla T}{T}. \quad (3)$$

The mass diffusion coefficient of species i in the mixture, $D_{i,m}$, is computed using Equation (4), where X_i is the mole fraction of species i. The binary mass diffusion coefficient of component i in component j is D_{ij}. It is defined by a modification of the Chapman-Enskog formula[23] using the kinetic theory, as given by Equation (5), where P_{abs} is the absolute pressure and $M_{w,i}$ is the molecular weight for species i. The diffusion collision integral, Ω_D, is a measure of the interaction of molecules within the system.[24]

TABLE I. Saturation vapor pressure and sublimation rate of powder MAI at different temperatures under an operating pressure of 20 mTorr.

Temperature (°C)	Saturation vapor pressure	Sublimation rate ($\times 10^{-9}$ g cm^2 s^{-1})
100	7 Pa = 0.053 Torr	1.24
120	40 Pa = 0.3 Torr	10.38
130	88 Pa = 0.66 Torr	23.44
150	385 Pa = 2.89 Torr	102.5
160	770 Pa = 5.78 Torr	203.4
180	2791 Pa = 20.9 Torr	722.5

TABLE II. Sublimation rate of powder MAI under different operating pressures at 150 °C.

Operating pressure (mTorr)	Sublimation rate ($\times 10^{-9}$ g cm^2 s^{-1})
10	102.8
20	102.5
30	102.1
40	101.8
50	101.4

$$D_{i,m} = \frac{1 - X_i}{\sum\limits_{j,j\neq i}(X_j/D_{ij})}, \quad (4)$$

$$D_{ij} = 0.00188\frac{\left[T^3\left(\dfrac{1}{M_{w,i}} + \dfrac{1}{M_{w,j}}\right)\right]^{1/2}}{P_{abs}\sigma_{ij}^2\Omega_D}, \quad (5)$$

Ω_D is a function of the quantity T_D^*, where

$$T_D^* = \frac{T}{(\varepsilon/k_B)_{ij}}, \quad (6)$$

in which k_B is the Boltzmann constant. For a mixture, $(\varepsilon/k_B)_{ij}$ is calculated by the geometric average

$$(\varepsilon/k_B)_{ij} = \sqrt{(\varepsilon/k_B)_i(\varepsilon/k_B)_j}. \quad (7)$$

For a binary mixture, σ_{ij} is calculated as the arithmetic average of the individual σ values

$$\sigma_{ij} = \frac{1}{2}(\sigma_i + \sigma_j). \quad (8)$$

Once the Lennard-Jones parameters, characteristic length, σ_i, and energy parameter, $(\varepsilon/k_B)_i$, have been defined for each species, the mass diffusion coefficient, $D_{i,m}$, is attained.

The kinetic theory is used in ANSYS Fluent to compute the thermal diffusion coefficient using the empirically based expression of Equation (9). No further inputs are required for this calculation.[25]

$$D_{T,i} = -2.59 \times 10^{-7}T^{0.659}\left[\frac{M_{w,i}^{0.511}X_i}{\sum\limits_{i=1}^{N}M_{w,i}^{0.511}X_i} - Y_i\right]$$

$$\times\left[\frac{\sum\limits_{i=1}^{N}M_{w,i}^{0.511}X_i}{\sum\limits_{i=1}^{N}M_{w,i}^{0.489}X_i}\right]. \quad (9)$$

A porous zone model is used to calculate the flow redistribution and pressure drop due to the porous screen. Specifically, a stainless steel woven screen is adopted owing to its excellent chemical stability and suitable thermal conductivity. Laminar flow is considered through the screen where the pressure drop is proportional to velocity (the

inertial resistance term of the porous medium model is set to zero). Ignoring convective acceleration and dispersion, the porous media model reduces to Darcy's law

$$\frac{\Delta P}{L} = -\frac{\mu}{K}u, \qquad (10)$$

where ΔP is the pressure drop, L is the thickness of woven screen, μ is the fluid dynamic viscosity, K is the permeability, $(1/K)$ is the viscous resistance, and u is the upstream fluid velocity. The pressure drop for fluid flow through screens is also usually written in the form[26,27]

$$\Delta P = \frac{1}{2}\zeta\rho u, \qquad (11)$$

where ρ is the density of the fluid and ζ is the resistance coefficient, a function of screen porosity, and the Reynolds number Re is

$$\text{Re} = \frac{u'd_0}{\nu}, \qquad (12)$$

where u' is the velocity based on the screen open area, $u = u'\beta$, where β is the open area ratio of the porous screen, d_0 is the diameter of equivalent hole of the woven screen, ν is the kinematic viscosity, and μ is the dynamic viscosity

$$\nu = \frac{\mu}{\rho}. \qquad (13)$$

For laminar flow, the Reynolds number should be very small, and the resistance coefficient can be determined from the following formulas:[27]

$$\zeta \approx \frac{22}{\text{Re}} + \zeta_{qu}, \qquad (14)$$

$$\zeta_{qu} = k_0(1-\beta) + \left(\frac{1}{\beta}-1\right)^2, \qquad (15)$$

where $k_0 = 1$ for wire screens. The value ζ_{qu} is so small that it can be ignored in this application. Therefore, the resistance coefficient simplifies to

$$\zeta \approx \frac{22}{\text{Re}}. \qquad (16)$$

Substituting Equations (12), (13), and (16) into Equation (11) gives

$$\Delta P = \frac{11\beta\mu u}{d_0}. \qquad (17)$$

Combining with Darcy's law, Equation (10), a relationship between permeability of the screen and the screen size can be obtained, as Equation (18). It can be used to choose the screen's mesh size to match the specific viscous resistance $(1/K)$

$$\frac{1}{K} = \frac{11\beta}{Ld_0}. \qquad (18)$$

The vapor-assisted deposition reaction of perovskite is defined by the Arrhenius reaction rate, Equation (19), where

A is the pre-exponential factor, E_a is the activation energy, and R is the universal gas constant. The Arrhenius equation gives the dependence of the rate constant k of a chemical reaction on the absolute temperature, T. The pre-exponential factor and activation energy of MAPbI$_3$ are 9×10^{15} and $110\,\text{kJ}\cdot\text{mol}^{-1}$, respectively,[28]

$$k = Ae^{-E_a/RT}. \qquad (19)$$

The reactant PbI$_2$ is absorbed onto the entire top surfaces of each substrate prior to the reaction with MAI vapor. Because little research has been done on the properties of vapor MAI, it is necessary to use the Joback estimating approach[29] to compute the specific heat, thermal conductivity, and viscosity of MAI vapor at a reference temperature of $80\,^\circ$C (353 K). For the Lennard-Jones (L-J) parameters of vapor MAI, an approximate general relation for the energy parameter is applied[30]

$$(\varepsilon/k_B) \approx 0.77T_c, \qquad (20)$$

where T_c is the critical temperature of vapor MAI, estimated to be $348.2\,^\circ$C (621.2 K) using the Joback method. The L-J energy parameter of vapor MAI is calculated to be $205.3\,^\circ$C (478.3 K). According to the Chapman-Enskog model,[31] the gas viscosity is found from

$$\mu = 2.669 \times 10^{-6} \frac{\sqrt{MT}}{\sigma^2\Omega_\mu}, \qquad (21)$$

where M is the molecular weight, σ is the L-J characteristic length, and Ω_μ is the collision integral for thermal conductivity which is calculated to be 1.88 here.[31] Then, the L-J characteristic length is reversely calculated using Equation (21) to be 5.2 Å. The corresponding properties of PbI$_2$ and MAPbI$_3$ defined in this work are listed in Table III.[30,32–34]

The quartz box walls are set to be a constant temperature to match the isothermal chamber condition in the actual experimental situation. The thermal boundary conditions of the substrates are set to be the vapor MAI zone temperature (above) and the temperature of quartz box walls (below). In addition, the symmetric simulation model in Figure 1(b) allows the same deposition situation on both left and right-side substrates.

TABLE III. Material properties of MAI, PbI$_2$, and perovskite MAPbI$_3$.

	MAI	PbI$_2$	MAPbI$_3$
Density (kg m^{-3})	Ideal gas	6160	4000
Specific heat (J kg^{-1} K^{-1})	498	173	304.85
Thermal conductivity (W m^{-1} K^{-1})	0.00672	0.73	0.5
Viscosity (kg m^{-1} s^{-1})	1.243×10^{-5}	1×10^{20}	1×10^{20}
Molecular weight (g mol^{-1})	159	461	620
Standard state enthalpy (J kmol^{-1})	-3.3×10^8	-2.03×10^8	-5.07×10^8
Standard state entropy (J kmol^{-1} K^{-1})	250 000	174 850	200 000
Reference temperature (K)	353	298.15	298.15
L-J characteristic length (Å)	5.2	5.5	6
L-J energy parameter (K)	478.3	400	550

Therefore, for simplicity, in the following discussions, only the calculation results of the left-side substrate are presented.

III. RESULTS AND DISCUSSION

A. Mass flow configuration

To achieve uniform perovskite layers using the vapor-assisted deposition method, it is critical to generate a steady and even mass flow distribution above the substrate surfaces. The simulation model in Figure 1(b) presents an effective mass flow configuration with three inlets and one middle outlet. Vapor MAI flows with a uniform flux from the three inlets into the box and exits from the middle outlet. The vapor MAI can react with the pre-coated PbI_2 on the substrate surface to produce perovskite $MAPbI_3$. Furthermore, if there are other two side outlets located off-center but symmetric about the center, a case with three inlets and three outlets is formed. Similarly, if the middle one of the three outlets is closed, leaving the two side outlets, a case with three inlets and two outlets is formed. In the same way, each of the three inlets can be set to be open or closed, allowing cases of one inlet and two inlets. Thus, nine different configurations are considered.

In this section, the influence of mass flow conditions on deposition uniformity is investigated with various inlet and outlet configurations. Figure 2 shows the influence of these configurations on the surface distribution of the deposition rate of perovskite $MAPbI_3$ on the left substrate. These depositions are based on the following operating conditions: temperature of $150\,°C$, outlet pressure of 20 mTorr, mass flux rate from the inlets of 102.5×10^{-9} g cm^2 s^{-1}, and viscous resistance of the porous screen of 3×10^6 m^{-2}. It is obvious that the configuration of three inlets and one outlet shows the best uniformity of the surface deposition rate. If the number of outlets is increased to two or three, the deposition rate decreases since more vapor MAI will exit from the chamber without reaction with the PbI_2. The uniformity also deteriorates because of the uneven mass fraction distribution. Furthermore, the cases of one inlet and two inlets present opposite distributions of the deposition rate due to opposing
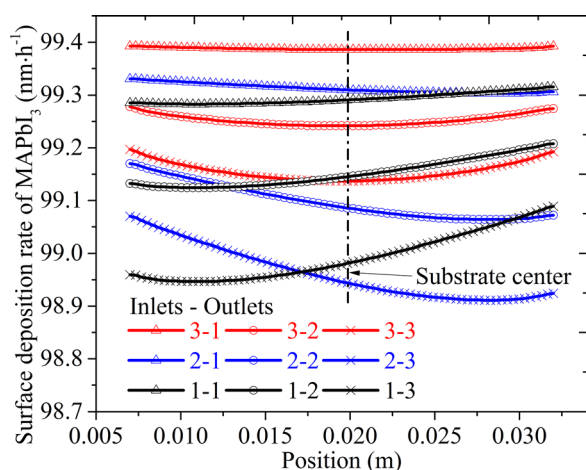
mass flow directions. In order to get a uniform perovskite layer, the structure of three inlets and one outlet is recommended.

Adding some resistance in the MAI mass flow path is an effective way to force a more uniform flow distribution to the substrate reaction zone. In our case, a porous screen is utilized. Figures 3(a) and 3(b) show the influence of porous screen viscous resistance based on the following operating conditions: three inlets and one outlet configuration, temperature of $150\,°C$, outlet pressure of 20 mTorr, and mass flux rate from the inlets of 102.5×10^{-9} g cm^2 s^{-1}. Without the
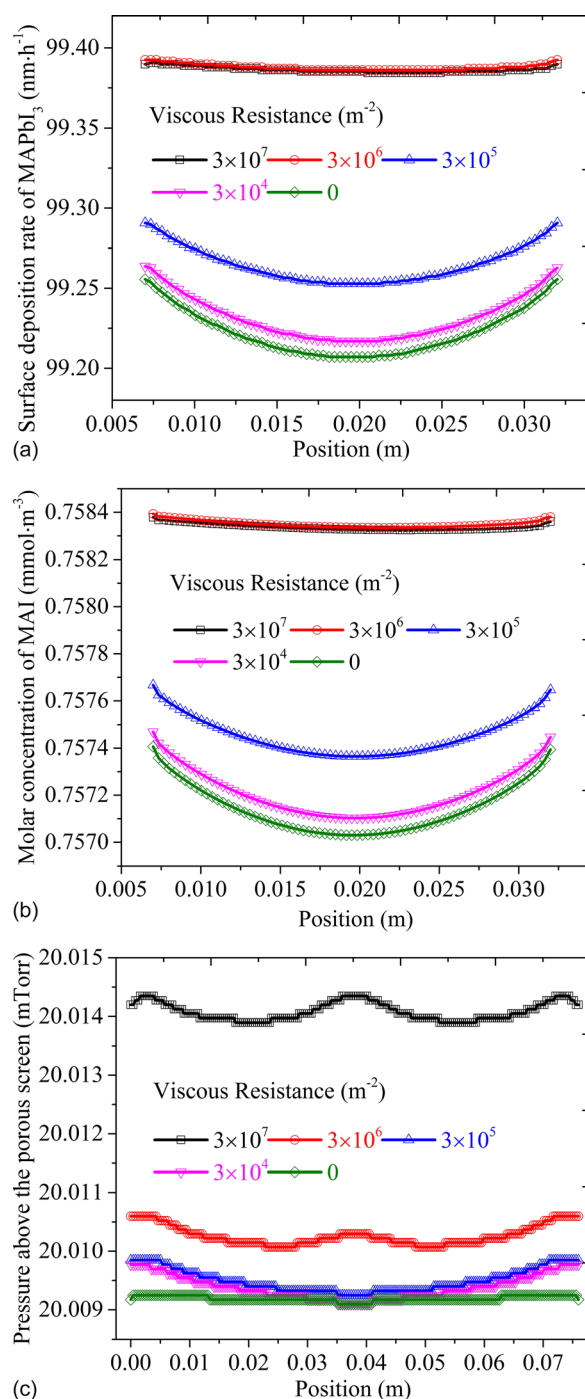

(a)

(b)

(c)

FIG. 3. The influence of porous screen viscous resistance on (a) surface distribution of the deposition rate of $MAPbI_3$ on the substrate; (b) surface distribution of the molar concentration of MAI; and (c) absolute pressure distribution at the inlet surface of the porous screen.

FIG. 2. Surface distribution of the deposition rate of $MAPbI_3$ with different mass flow configurations.

screen (viscous resistance equals to 0), the MAI distribution and deposition rate of perovskite are uneven. It becomes very uniform when the screen viscous resistance is increased to 3×10^6 or $3 \times 10^7 \, m^{-2}$, while the deposition rate on the entire substrate is essentially unchanged. However, when the viscous resistance is further increased to a magnitude of 10^8 or 10^9, the simulation becomes non-convergent and presents backflow from the outlet. This suggests that it may be a condition to be avoided in practical experiments. In addition, with high viscous resistance, more MAI is restricted above the porous screen until its saturation, causing an increase in the pressure above the porous screen, as shown in Figure 3(b). A viscous resistance of $3 \times 10^6 \, m^{-2}$ is adopted in the following calculation, which can be attained practically by using a 20×20 mesh (20 mesh features per inch), with a wire diameter of 0.508 mm, the square open area length of 0.15 mm, and the porosity of 36%. A finer mesh screen is needed to get a viscous resistance of $3 \times 10^7 \, m^{-2}$, for example, a mesh size of 100×100, with a wire diameter of 0.102 mm and the square open area length of 0.15 mm, giving the porosity of 36%.

Almost all the current research on perovskite solar cells is focused on improving the power conversion efficiency and

stability. However, reproducibility and large-scale area are other essential factors to successful commercial production of perovskite solar cells, which needs really uniform perovskite films. According to the above discussion, one can reproducibly achieve uniform perovskite films using the selected configuration with a porous screen embedded in the mass flow path.

B. Temperature

Temperature is the most critical factor affecting the perovskite deposition process. In this section, the influence of operating temperature is discussed. It is obtained by both steady and transient calculations with three inlets and one outlet configuration, a porous screen resistance of $3 \times 10^6 \, m^{-2}$, and an outlet pressure of 20 mTorr. The mass flux rates from the inlets at different temperatures are based on the data given in Table I. With the increase in working temperature, the sublimation rate of MAI increases accordingly.

1. Steady calculations

As shown in Figures 4(a), 4(c), and 4(e), regardless of operating temperature, the steady deposition rate of perovskite
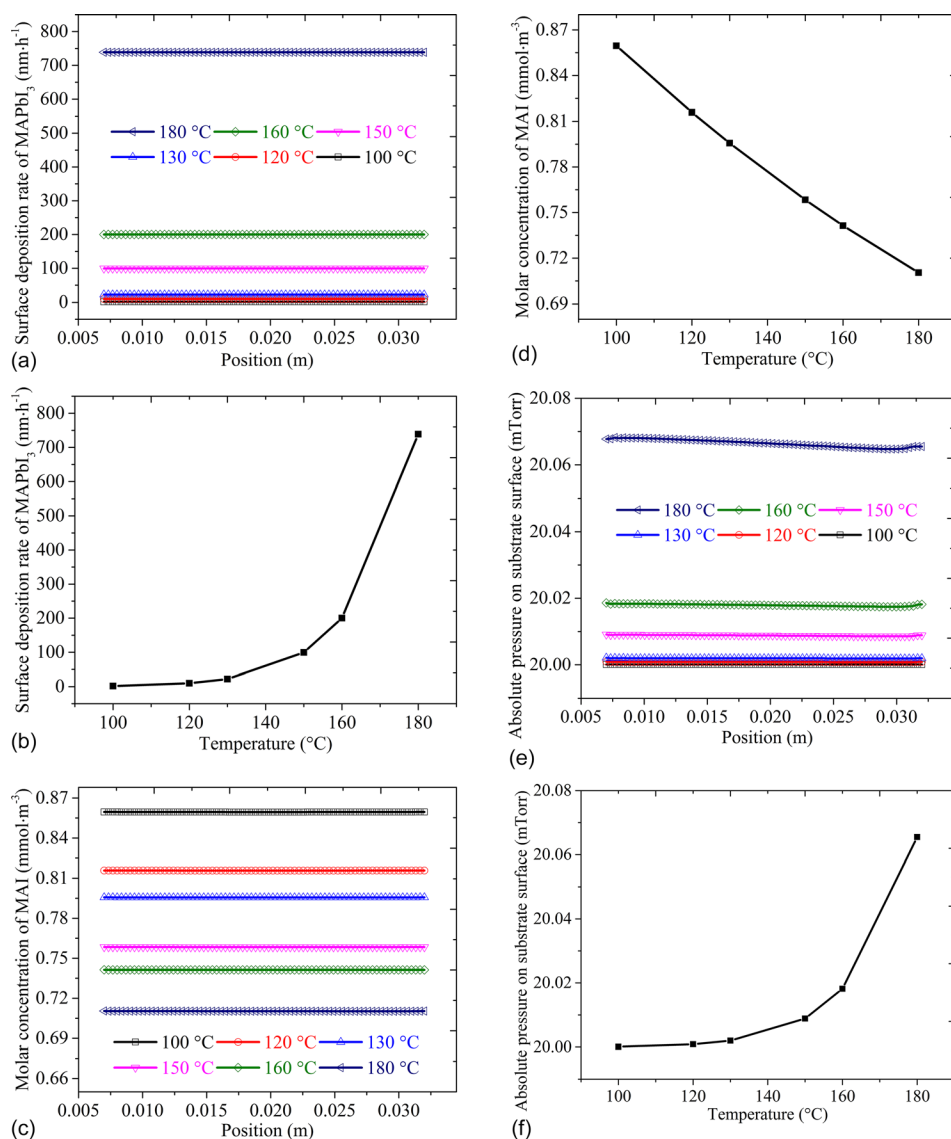

FIG. 4. Steady calculation results on the substrate surface. (a) Surface distribution of the deposition rate of MAPbI$_3$. (b) Average deposition rate of MAPbI$_3$ with respect to temperatures. (c) Surface distribution of the molar concentration of MAI. (d) Average molar concentration of MAI with respect to temperatures. (e) Surface distribution of the absolute pressure. (f) Average pressure with respect to temperatures.

$MAPbI_3$, the molar concentration of MAI, and the absolute pressure are uniform across the substrate surface. This is attributed to the choice of inlets, outlets, and the porous screen design. In addition, Figures 4(b) and 4(f) show that with increasing working temperature, the deposition rate and absolute pressure on the substrate surface increase.

However, the molar concentration of MAI decreases almost linearly with increasing temperature, although the sublimation rate of MAI increases with increasing temperature. This is because a fast perovskite deposition rate at high temperatures leads to vastly larger consumption of vapor MAI at the substrate surface. The concentration gradient of MAI vapor above the substrate surface increases, which, in turn, leads to a high deposition rate of perovskite films. In addition, the ideal gas state equation shows that

$$PV = nRT. \tag{22}$$

If operating pressure, P, and quartz box volume, V, are fixed, the number of moles, n, is inversely proportional to the temperature, T. As seen in Figure 4(f), the pressure on the substrate increases less than 1 mTorr with increasing temperature from $100\,°C$ to $180\,°C$. Thus, the pressure P is essentially constant in some extent. Based on Equation (22), the molecular concentration, n/V, is inversely proportional to the temperature, T.

2. Transient calculations

As can be seen in the steady calculations, changing temperature just changes the deposition rate of perovskite films, while no influence on the deposition uniformity over the entire substrate. Transient calculation is conducted to further illustrate the perovskite deposition process at a temperature of $150\,°C$ and an outlet pressure of 20 mTorr. As shown in

Figure 5, the surface deposition rate of perovskite becomes uniform and stable with time. Initially, the chamber is filled with N_2. The molar concentration of MAI increases as MAI flows onto the substrate and N_2 is purged. In addition, the porous screen forces the MAI vapor flow to become well-distributed before passing through, and MAI expands progressively more uniformly over the substrate. Throughout the transient, MAI is consumed by the deposition reaction, dropping the average pressure on the substrate surface. Finally, a stable pressure that is higher than the outlet pressure of 20 mTorr is attained and is maintained with stable mass flow and uniform perovskite film growth.

Figure 6 illustrates the path lines from the three inlets, colored by the molar concentration of MAI, for various times during the transient calculation. It clearly presents how the porous screen is very useful in forcing a well-distributed mass flow, giving uniform MAI coverage on the substrate surface. With time, more and more path lines are directed toward the substrate surface. Eventually, a stable point is reached and the deposition rate becomes steady. In addition, the molar concentration gradient of MAI in the box progressively decreases while N_2 is removed from the box, leaving the uniformly distributed MAI to deposit on the substrate surface. Nevertheless, the concentration of MAI around the substrate still shows slight differences, causing slight pressure differences across the substrate, as seen in Figures 4(e) and 5(c). In the meantime, the small concentration and pressure differences are essential for having steady vapor flow to the outlet, to maintain a stable deposition reaction.

C. Outlet pressure

Pressure is another critical factor influencing the deposition process. In this section, the influence of operating pressure
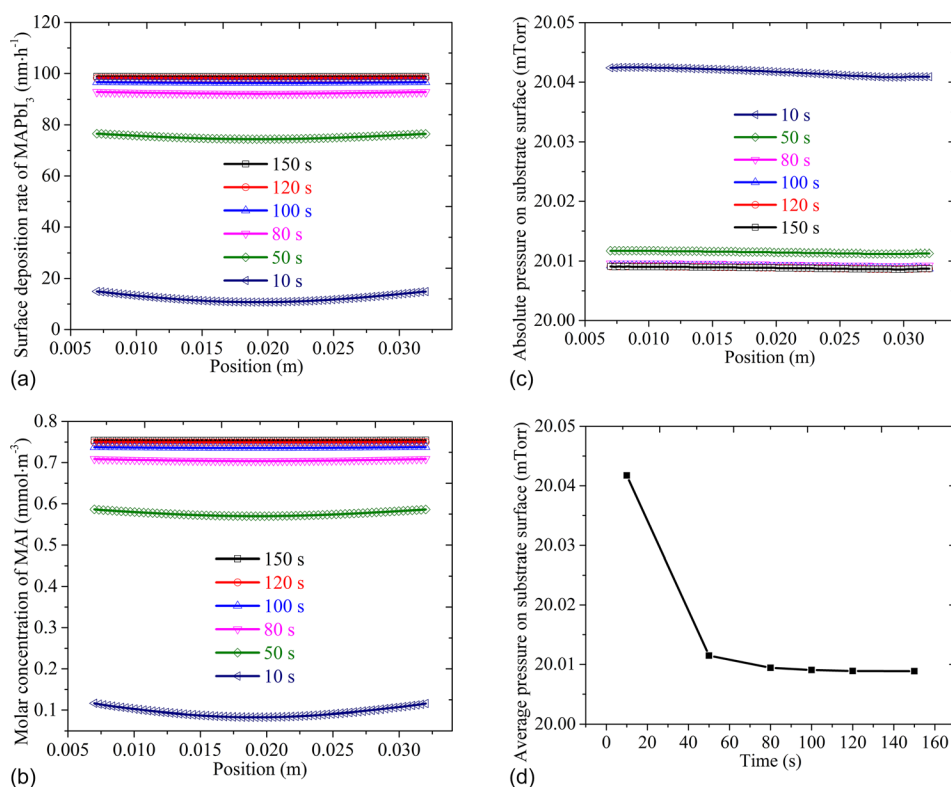
FIG. 5. Transient calculation results on the substrate surface at $150\,°C$. (a) Surface distribution of the deposition rate of $MAPbI_3$. (b) Surface distribution of the molar concentration of MAI. (c) Surface distribution of the absolute pressure. (d) Average pressure with respect to time.
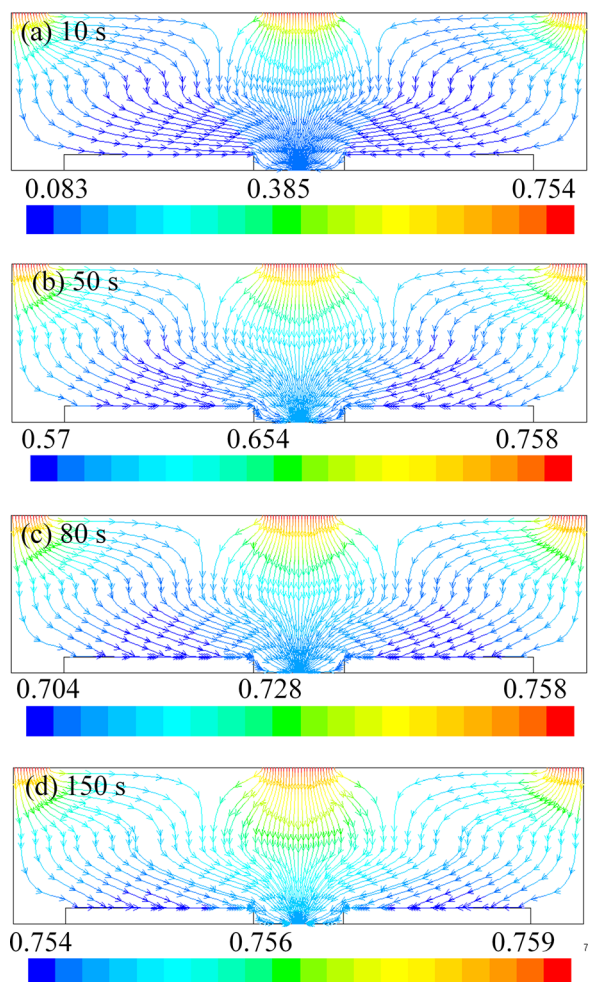
FIG. 6. Path lines colored by the molar concentration of MAI (mmol m^{-3}) in transient calculation at 150 °C. (a) 10 s, (b) 50 s, (c) 80 s, and (d) 150 s.

on perovskite deposition is quantified. All cases are steady and analyzed with three inlets and one outlet configuration, a porous screen resistance of 3×10^6 m^{-2}, and a temperature of 150 °C. Mass flow rates from the inlets are based on the data given in Table II. With different pressures, Figure 7 shows a uniform deposition rate of perovskite MAPbI$_3$, a uniform molar concentration of MAI at the substrate, and uniform absolute pressure over the substrate surface. In addition, the molar concentration of MAI and the vapor pressure inside the quartz box increase with an increase in outlet pressure, regardless of the slightly declining sublimation rate of MAI. The reason is that the box with increasing pressure can accommodate more MAI vapor molecules, while at the steady state with enough time to let the MAI sublimate and assemble to saturation, so that the concentration of MAI and pressure above the substrate increase. Furthermore, the pressure difference between the substrate surface and the outlet reduces gradually with increasing outlet pressure. Under critical conditions, the pressure around the outlet will be equal to the pre-set outlet pressure. Increasing pressure further will lead to backflow, causing a nonuniform deposition rate and the introduction of contaminates to the chamber. The backflow should to be avoided.

According to Equation (19), the deposition reaction rate is independent of pressure. However, according to Fick's laws, Equation (3), when working temperature is fixed, the
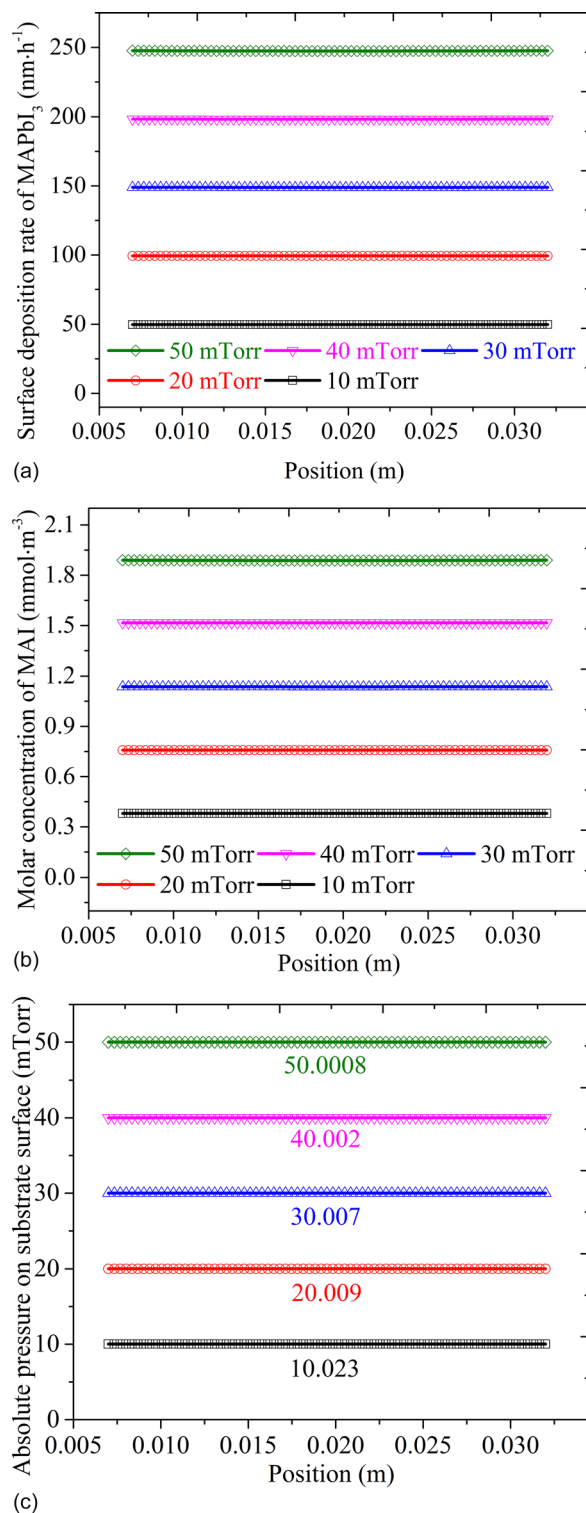

FIG. 7. Steady calculation results on the substrate surface with respect to different outlet pressures. (a) Surface distribution of the deposition rate of MAPbI$_3$. (b) Surface distribution of the molar concentration of MAI. (c) Surface distribution of the absolute pressure.

diffusion flux is mainly depended on the concentration gradient.[35] With increasing working pressure, the concentration and partial pressure of MAI vapor increase, increasing the concentration gradient of MAI vapor above the substrate surface. This explains why the perovskite film grows faster with increasing working pressure.

IV. CONCLUSIONS

Numerical simulation and analysis of hybrid physical-chemical vapor deposition of perovskite $MAPbI_3$ were investigated using ANSYS Fluent software. It was shown that a homogeneous mass flow distribution of MAI vapor could be achieved under proper conditions, leading to a perovskite layer with uniform thickness. This was attained by utilizing an optimized mass flow configuration with three inlets and one outlet and the addition of a suitably selected porous screen. Both steady and transient calculations were conducted to study the heat and mass transfer during the perovskite deposition process. The results show that the surface deposition rate of perovskite $MAPbI_3$ increases with increasing operating temperature and pressure. At high temperatures, MAI vapor sublimates more rapidly, partially balancing its consumption in the perovskite films. However, with increasing working pressure, the sublimation rate of MAI reduces, decreasing MAI vapor supply to the deposition of perovskite films. If the working conditions surpass a critical pressure, reverse flow takes place from the outlet, deteriorating the uniformity of MAI concentration distribution on the substrate surface, inducing an uneven deposition of perovskite films and ingesting contaminants. The temperature, pressure, and the sublimation mass flux rate are all closely interrelated. The model in the present paper sets criteria to avoid backflow. Well-controlled operating conditions are essential to realizing uniform, stable, and reproducible perovskite films by hybrid physical-chemical vapor deposition. This work paves the way toward producing high quality perovskite layers in perovskite-based devices, such as solar cells, photodetectors, and Light-emitting diodes (LEDs).

ACKNOWLEDGMENTS

[1]M. Saliba, T. Matsui, J.-Y. Seo, K. Domanski, J.-P. Correa-Baena, M. K. Nazeeruddin, S. M. Zakeeruddin, W. Tress, A. Abate, A. Hagfeldt, and M. Gratzel, Energy Environ. Sci. **9**, 1989 (2016).
[2]A. Kojima, K. Teshima, Y. Shirai, and T. Miyasaka, J. Am. Chem. Soc. **131**, 6050 (2009).
[3]See http://www.nrel.gov/pv/assets/images/efficiency_chart.jpg for NREL Chart, 2016 (last accessed March 13, 2017).
[4]M. M. Lee, J. Teuscher, T. Miyasaka, T. N. Murakami, and H. J. Snaith, Science **338**, 643 (2012).
[5]P. Docampo, J. M. Ball, M. Darwich, G. E. Eperon, and H. J. Snaith, Nat. Commun. **4**, 2761 (2013).
[6]J. You, Z. Hong, Y. M. Yang, Q. Chen, M. Cai, T.-B. Song, C.-C. Chen, S. Lu, Y. Liu, and H. Zhou, ACS Nano **8**, 1674 (2014).
[7]P. Docampo and T. Bein, Acc. Chem. Res. **49**, 339 (2016).
[8]Y. Zhao and K. Zhu, Chem. Soc. Rev. **45**, 655 (2016).
[9]Q. Chen, H. Zhou, Z. Hong, S. Luo, H.-S. Duan, H.-H. Wang, Y. Liu, G. Li, and Y. Yang, J. Am. Chem. Soc. **136**, 622 (2014).
[10]Y. Li, J. K. Cooper, R. Buonsanti, C. Giannini, Y. Liu, F. M. Toma, and I. D. Sharp, J. Phys. Chem. Lett. **6**, 493 (2015).
[11]Y. Peng, G. Jing, and T. Cui, J. Mater. Chem. A **3**, 12436 (2015).
[12]Y. Peng, G. Jing, and T. Cui, RSC Adv. **5**, 95847 (2015).
[13]S.-Y. Hsiao, H.-L. Lin, W.-H. Lee, W.-L. Tsai, K.-M. Chiang, W.-Y. Liao, C.-Z. Ren-Wu, C.-Y. Chen, and H.-W. Lin, Adv. Mater. **28**, 7013 (2016).
[14]J. Yin, H. Qu, J. Cao, H. Tai, J. Li, and N. Zheng, J. Mater. Chem. A **4**, 13203 (2016).
[15]C. Yi, X. Li, J. Luo, S. M. Zakeeruddin, and M. Grätzel, Adv. Mater. **28**, 2964 (2016).
[16]Y. Jo, K. S. Oh, M. Kim, K.-H. Kim, H. Lee, C.-W. Lee, and D. S. Kim, Adv. Mater. Interfaces **3**, 1500768 (2016).
[17]W. S. Yang, J. H. Noh, N. J. Jeon, Y. C. Kim, S. Ryu, J. Seo, and S. I. Seok, Science **348**, 1234 (2015).
[18]I. Langmuir, J. Am. Chem. Soc. **40**, 1361 (1918).
[19]S. Miyamoto, Trans. Faraday Soc. **29**, 794 (1933).
[20]A. Dualeh, P. Gao, S. I. Seok, M. K. Nazeeruddin, and M. Grätzel, Chem. Mater. **26**, 6160 (2014).
[21]J. K. Platten, J. Appl. Mech. **73**, 5 (2006).
[22]J. Weickert, *Scale-Space Theory in Computer Vision* (Springer, 1997), p. 1.
[23]H. A. McGee, *Molecular Engineering* (McGraw Hill, New York, 1991).
[24]P. D. Neufeld, A. R. Janzen, and R. A. Aziz, J. Chem. Phys. **57**, 1100 (1972).
[25]K. Kuo, *Principles of Combustion*, 2nd ed. (Wiley Interscience, New York, 1986).
[26]A. Valli, J. Hyväluoma, A. Jäsberg, A. Koponen, and J. Timonen, Transp. Porous Media **80**, 193 (2009).
[27]I. E. Idel'chik and M. O. Steinberg, *Handbook of Hydraulic Resistance*, 4th ed. (Begell House, New York, 1996).
[28]B. Wang, K. Young Wong, X. Xiao, and T. Chen, Sci. Rep. **5**, 10557 (2015).
[29]K. G. Joback and R. C. Reid, Chem. Eng. Commun. **57**, 233 (1987).
[30]C. F. Curtiss, J. O. Hirschfelder, and R. B. Bird, *Molecular Theory of Gases and Liquids* (John Wiley & Sons, New York, 1954).
[31]S. M. Ghiaasiaan, *Convective Heat and Mass Transfer* (Cambridge University Press, New York, USA, 2011).
[32]N. Onoda-Yamamuro, T. Matsuo, and H. Suga, J. Phys. Chem. Solids **51**, 1383 (1990).
[33]A. Pisoni, J. Jaćimović, O. S. Barišić, M. Spina, R. Gaál, L. Forró, and E. Horváth, J. Phys. Chem. Lett. **5**, 2488 (2014).
[34]J. Tonn, Ph.D. thesis, Albert-Ludwigs-University of Freiburg, 2012.
[35]P. L. Durrill and R. G. Griskey, AIChE J. **15**, 106 (1969).